Progress In Electromagnetics Research M, Vol. 105, 55–65, 2021

Performance Comparison of Spoke Array Fault Tolerant PM Vernier Rim Driven Machine with Different Numbers of Flux Modulation Poles

Tianhuai Qiao, Jingwei Zhu*, and Xiaoyi Wang

Abstract—In this paper, the effect of flux modulation pole (FMP) number on the performance of a spoke array fault tolerant permanent magnet vernier rim driven machine (SA-FTPMV-RDM) is studied. Firstly, a hybrid stator is adopted in this machine in which armature teeth and isolation teeth are arranged alternatively, and the winding type is single-layer fractional slot concentrated winding (SL-FSCW). Spoke array magnet is employed in the rotor of the machine to achieve flux focusing effect. Then the parameter scanning method is used to optimize the FMP pitch ratio, isolation tooth width ratio, FMP height, and permanent magnet thickness under different numbers of FMPs. It is concluded that there is an optimal FMP number for 12 slots SA-FTPMV-RDM to maximize the torque. Finally, the electromagnetic performances of the optimized machines with different number of FMP are compared by using the finite element analysis (FEA). The results show that the machine with the optimal number of FMPs has the highest torque density and efficiency, strong fault tolerance, but relatively large torque ripple.

1. INTRODUCTION

In recent years, rim driven thruster (RDT) has attracted more and more attention because of its advantages of high integration, high efficiency, and low noise [1–3]. At present, the built-in machines of RDT are mainly brushless DC machine and permanent magnet synchronous machine (PMSM), but the increase of air gap length which is 2–3 times that of traditional PM machines weakens the torque density of RDT. In the meantime, distributed windings are usually adopted and do not have fault tolerance [4, 5]. The RDT needs to operate underwater for a long time, which requires it to have strong fault tolerant capability. With the advantages of simple structure and high torque density, the permanent magnet vernier machine (PMVM) based on the principle of magnetic gearing effect has been gradually becoming the primary choice for low-speed and high torque applications [6, 7]. The combination of PMVM and RDT can significantly improve the torque performance of RDT.

The topology of PMV machine has always been a research hotspot. Its stator structure mainly includes open slots [8] and split teeth [9]. Distributed winding is generally adopted in an open slot structure, which is characterized by high output torque, but the winding end length is too long, so the copper loss will be relatively high, and there is no fault tolerance. Concentrated winding is usually employed in split tooth structure, which is featured by short winding end length, low copper loss, and strong fault tolerant capability, but contribute to torque reduction. Therefore, how to improve the output torque of the machine under a split tooth structure with concentrated winding has become a key point.

Received 26 August 2021, Accepted 1 October 2021, Scheduled 10 October 2021
* Corresponding author: Jingwei Zhu (zjwdl@dlmu.edu.cn).
The authors are with the College of Marine Electrical Engineering, Dalian Maritime University, Dalian 116026, China.

The arrangements of rotor PMs mainly include surface mounted [10], consequent pole [11], Halbach array [12], spoke array [13], etc. PMVM with a spoke array has high torque density due to its flux concentration. In [14], the working principle of PMVM with open slots structure and spoke arrays is analyzed by analytical method for the first time, and it is pointed out that the vernier effect will be greatly weakened with high pole ratio, which is called flux barrier effect. A split tooth structure is studied in [15], and it is found that the uneven distribution of flux modulation poles (FMPs) can lead to multi-harmonic flux modulation effect and hence improve the torque density. In [16], a split tooth structure is combined with a spoke array, and a hybrid stator fault tolerant PMVM is proposed. It is pointed out that its torque density is about 40% higher than the surface mounted type, but it is only limited to the case that the number of FMPs on each armature tooth is 2. At present, the performance comparison of hybrid stator spoke array fault tolerant PM vernier rim driven machines (SA-FTPMV-RDMs) with different numbers of FMPs is not reported. Moreover, the influence of geometric size on SA-FTPMV-RDM with different numbers of FMPs has not been investigated. In Section 2, the topology of SA-FTPMV-RDM will be introduced, and the working principle will be analyzed. The influences of structure parameters on machine performance will be presented in Section 3. The performance comparison will be discussed in Section 4. The conclusion will be drawn in Section 5.

2. MACHINE TOPOLOGY AND WORKING PRINCIPLE

2.1. Machine Topology

The SA-FTPMV-RDM with different numbers of FMPs proposed in this paper are shown in Figs. 1(a)–(d). The number of FMPs on each armature tooth is N_f. When $N_f = 1$, the machine is a traditional SA-FTPM-RDM, which has almost no flux modulation effect. When $N_f > 1$, the machine works according to the flux modulation effect, which is an SA-FTPMV-RDM. The cases of $N_f = 2$, 3, 4, 5 are mainly investigated in this paper. The rotor of SA-FTPMV-RDM is a spoke array structure in which permanent magnet is magnetized tangentially, and the magnetization directions of two adjacent permanent magnets are opposite. In addition, a hybrid stator with 12 slots is adopted, and armature teeth and isolation teeth are arranged alternatively. Split teeth are placed on each armature tooth, and each isolation tooth is regarded as a split tooth. All split teeth work as FMPs to modulate the air gap magnetic field to achieve low-speed and high torque output. Moreover, six phase single-layer fractional slot concentrated winding (SL-FSCW) is used in this machine, which not only enhances the fault tolerance of the machine, but also reduces the end length of the winding and the copper loss.

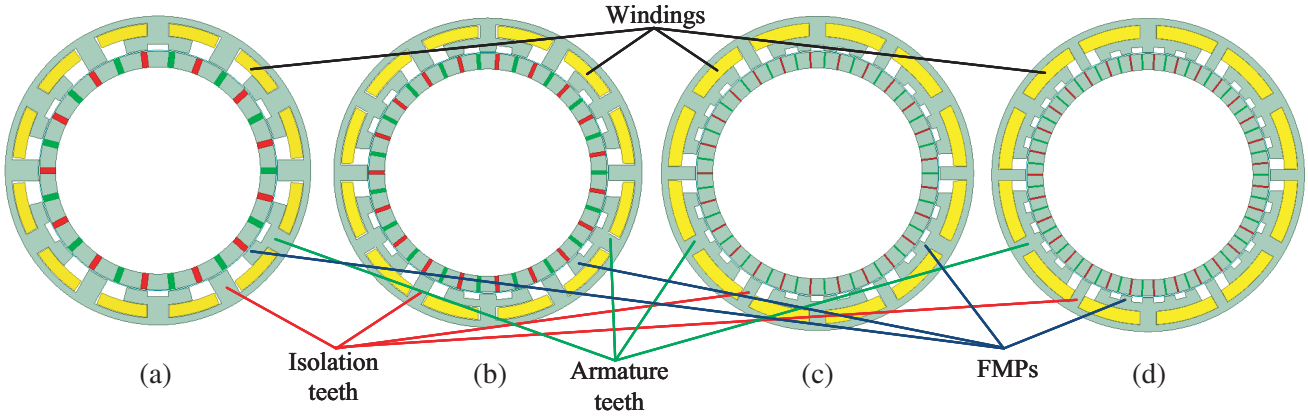

Figure 1. Cross sections of SA-FTPMV-RDM. (a) $N_f = 2$. (b) $N_f = 3$. (c) $N_f = 4$. (d) $N_f = 5$.

2.2. Working Principle

Similar to the traditional PMVM, the working principle of SA-FTPMV-RDM is still magnetic field modulation effect. In order to obtain high output torque, the number of FMPs Z_s, the PMs pole pair

number P_r, and the pole pair number of armature windings P_w meet the following relationship:

$$Z_s = P_r + P_w \tag{1}$$

The relationship between the number of armature teeth Z_a, Z_s, and the number of FMPs on each armature tooth N_f is governed by:

$$Z_s = (N_f + 1) Z_a \tag{2}$$

The air gap flux density harmonics $P_{m,n}$, Z_s, and P_r satisfy:

$$P_{m,n} = |mP_r \pm nZ_s| \quad m = 1, 3, 5, \ldots \quad n = 0, 1, 2, \ldots \tag{3}$$

The angular velocity of the air gap flux density harmonics can be expressed as:

$$\omega_{m,n} = \frac{mP_r}{mP_r \pm nZ_s}\omega_r \tag{4}$$

where ω_r is the mechanical angular velocity of the rotor. when $m = 1$ and $n = 0$, the fundamental harmonic of air gap flux density is generated which has the highest amplitude, and $\omega_{1,0} = \omega_r$. When $m = 1$, $n = 1$, and the negative sign holds, the air gap flux density harmonic $P_{1,-1}$ has the smallest pole pair number and the highest angular velocity. The utilization of air gap flux density harmonics and torque can be maximized by making $P_w = P_{1,-1}$.

The pole ratio of SA-FTPMV-RDM can be defined as follows:

$$G_r = \frac{\omega_{m,n}}{\omega_{1,0}} = \frac{mP_r}{|mP_r \pm nZ_s|} \tag{5}$$

The pole ratio is the highest when $m = 1$, $n = 1$, and the negative sign holds, and it is worth noting that $\omega_{1,-1}$ and ω_r rotate in the opposite directions.

3. OPTIMIZATION OF SA-FTPMV-RDM

In this section, the parameter scanning method is mainly used to optimize the four machines with $N_f = 2$, 3, 4, and 5. The schematic diagram of simplified structural parameters of machine is presented in Fig. 2. The initial design parameters are shown in Table 1. The FMPs pitch ratio, isolation tooth width ratio, the height of FMPs, and the permanent magnet thickness are selected to optimize for the maximum output torque and minimum torque ripple. During the optimization process, the main size and electrical load of four machines remain unchanged.

Table 1. Initial design parameters of four machines.

Items	$N_f = 2$	$N_f = 3$	$N_f = 4$	$N_f = 5$
Number of FMPs	18	24	30	36
PMs pole pair number	13	19	25	31
Stator outer diameter (mm)	255			
Rotor inner diameter (mm)	171			
Air gap length (mm)	1.5			
Axial length (mm)	45			
W_f/τ_f	0.5			
W_g/τ_g	0.5			
Height of FMPs (mm)	4			
Winding turns per phase	300			
Remanence of PM, Br (T)	1.23			
PM thickness (mm)	1.0			

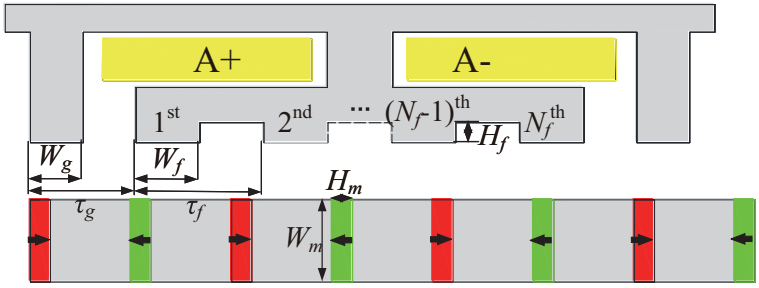

Figure 2. Schematic of simplified structural parameters of SA-FTPMV-RDM.

3.1. FMPs Pitch Ratio Optimization

As shown in Fig. 2, when FMPs are uniformly distributed, $W_f = W_g = 0.5\tau_f = 0.5\tau_g$, the angle between two adjacent FMPs is expressed as:

$$\tau_f = \tau_s = \frac{2\pi}{Z_s} \tag{6}$$

When FMPs are non-uniformly distributed, τ_f is different from τ_s. The FMPs pitch ratio and isolation tooth width ratio are respectively defined as: τ_f/τ_s and τ_g/τ_s. Furthermore, H_f and H_m are the height of FMPs and magnet thickness, respectively. The initial values of τ_f/τ_s, τ_g/τ_s, H_f, and H_m of four machines are 1, 1, 4 mm, and 1 mm, respectively. During the optimization of τ_f/τ_s, the values of H_f and H_m were kept at 4 mm and 1 mm, respectively. Fig. 3(a) shows the effect of τ_f/τ_s on torque. It can be seen that as τ_f/τ_s increases, the torque gets larger at first due to the multiple working harmonics, but it gets smaller afterwards because of the increase of equivalent air gap length. The optimal values of τ_f/τ_s for maximum torque of four machines are 1.3, 1.2, 1.15, and 1.1, respectively. With the increase of pole ratio, the optimal τ_f/τ_s decreases gradually. After that, the influence of τ_f/τ_s on torque ripple is presented in Fig. 3(b). With the change of τ_f/τ_s, the torque ripple of the four machines shows a fluctuating trend. Besides, the torque ripple with $N_f = 5$ is the smallest due to its largest number of slots and poles.

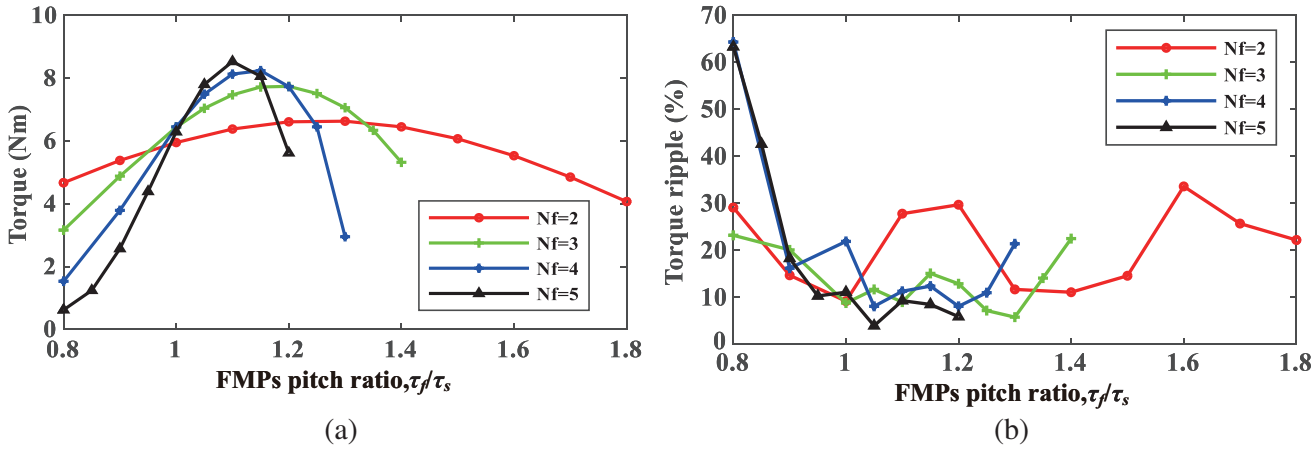

(a) (b)

Figure 3. Effect of FMPs pitch ratio on torque performances. (a) Torque. (b) Torque ripple.

3.2. Isolation Tooth Width Ratio Optimization

When τ_g/τ_s is optimized, τ_f/τ_s is equal to its corresponding optimal value, while the values of H_f and H_m were kept as 0 mm and 4 mm, respectively. The influence of τ_g/τ_s on torque is illustrated in Fig. 4(a). It can be found that the torque increases with τ_g/τ_s in the first place, due to the enhancing flux

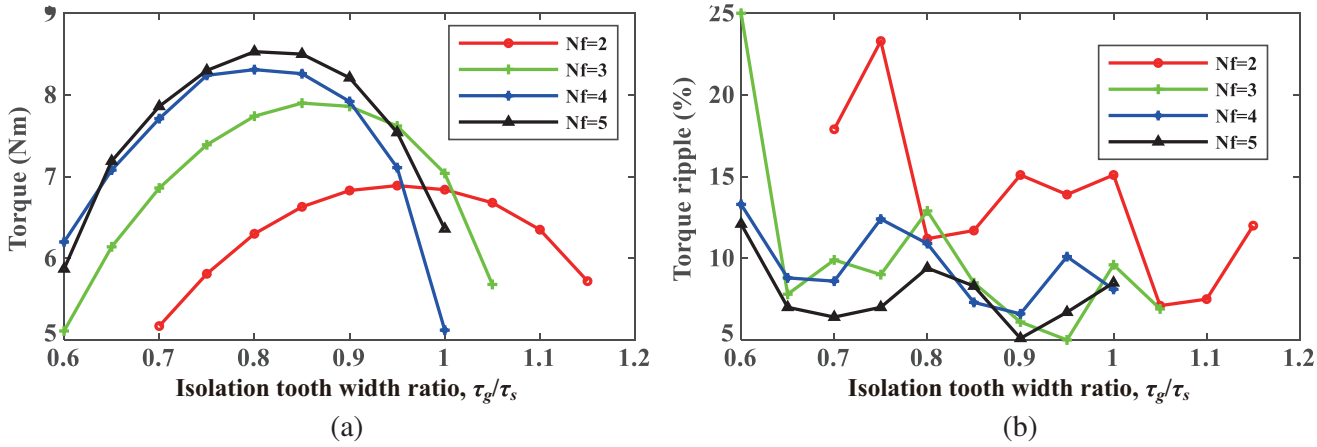

Figure 4. Influence of isolation tooth width ratio on torque performances. (a) Torque. (b) Torque ripple.

modulation effect. However, when crossing the optimal point of τ_g/τ_s, the torque decreases gradually. The optimal values of τ_g/τ_s for the maximum torque of four machines are 0.95, 0.85, 0.8, and 0.8, respectively. Moreover, the optimal τ_g/τ_s gets smaller with increased pole ratio. Furthermore, Fig. 4(b) depicts the effect of τ_g/τ_s on torque ripple. As will be seen, there is no clear variation rule between the torque ripple and τ_g/τ_s of the four machines, but there is an optimal value. The optimal values of τ_g/τ_s for minimum torque ripple of four machines are 1.05, 0.95, 0.9, and 0.9, respectively, which means that a compromise is needed to obtain the maximum torque and minimum torque ripple.

3.3. Height of FMPs Optimization

In the optimization process of H_f, the value of H_m is chosen as 1 mm, while τ_f/τ_s and τ_g/τ_s are kept as their corresponding optimal values, respectively. The influence of H_f on torque is revealed in Fig. 5(a). It is interesting to conclude that the torque increases with H_f in the beginning, owing to the stronger field modulation effect. After the torque reaches the maximum value, the torque decreases gradually with H_f due to the saturation of stator teeth. The optimal values of H_f for maximum torque of four machines are 5.5 mm, 6 mm, 5.5 mm, and 5 mm respectively. In addition, Fig. 5(b) analyzes the effect of H_f on torque ripple. It can be found that torque ripple hardly changes with H_f when $N_f = 3$, 4, and 5, while it has an optimal value when $N_f = 2$. Besides, the torque variation of four machines is relatively small in the whole optimization process, indicating that H_f has little effect on torque performance.

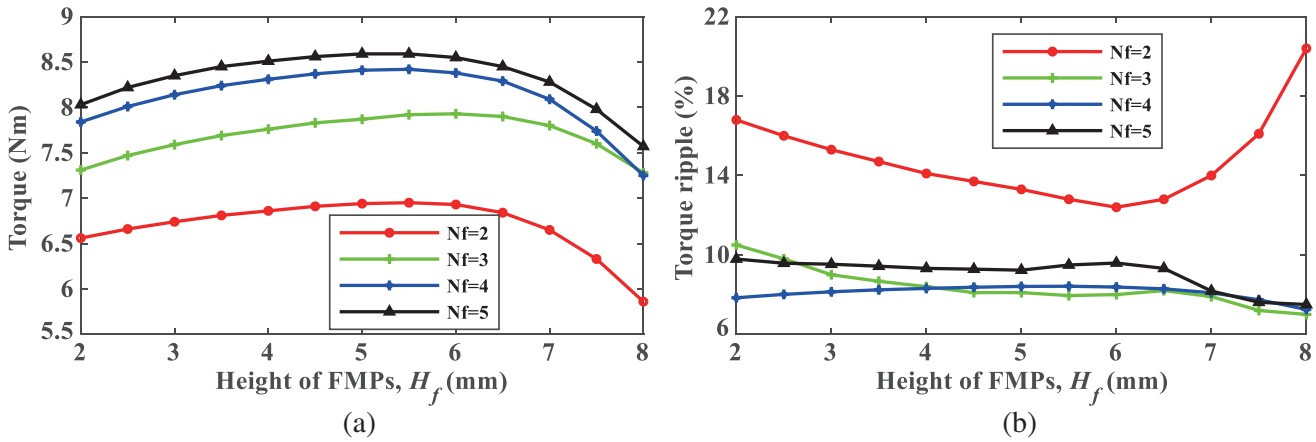

Figure 5. Influence of height of FMPs on torque performances. (a) Torque. (b) Torque ripple.

3.4. Magnet Thickness Optimization

In this paper, only H_m needs to be optimized because of the fixed W_m. τ_f/τ_s, τ_g/τ_s, and H_f adopt their respective optimal values during the optimal design process of H_m. The effect of H_m on torque of four machines is shown in Fig. 6(a). It can be noted that the torque rises with H_m in the initial stage thanks to the stronger air gap flux density. When crossing the optimal point of H_m, the torque declines step by step for the saturation of rotor pieces. The values of H_m optimized for maximum torque are 13.5 mm, 10 mm, 7.5 mm, and 6 mm, respectively. Moreover, Fig. 6(b) presents the influence of H_m on torque ripple. It is not hard to find that torque ripple fluctuates with the increase of H_m, but the minimum torque ripple and the corresponding H_m can be determined. The optimal values of H_m for minimum torque ripple of four machines are 9 mm, 6 mm, 4 mm, and 3.5 mm, respectively, which indicates that a comprehensive consideration is required to obtain the maximum torque and minimum torque ripple.

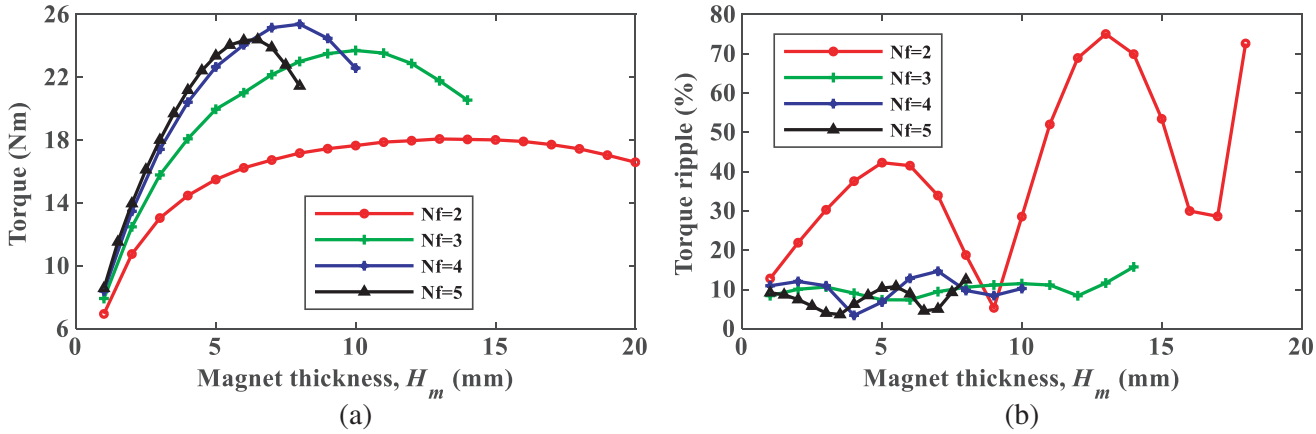

Figure 6. Influence of magnet thickness on torque performances. (a) Torque. (b) Torque ripple.

4. PERFORMANCE COMPARISON BY FEA

Based on the above analysis, it can be concluded that there is an optimal N_f for the six-phase 12-slot SA-FTPMV-RDM to maximize its torque, and the optimal N_f is determined as 4 in this paper. Additionally, τ_f/τ_s, τ_g/τ_s, and H_m have obvious effects on output torque, while H_f has little influence on torque. The optimized parameters of the four machines founded on the maximum torque are summarized in Table 2. In this section, comparative analysis of electromagnetic performance under the optimal parameters of four machines will be performed by FEA. The simulation is used by Ansoft Maxwell 16.0 transient analysis, and the number of finite elements of four models are 62848, 63950, 65664, and 66882, respectively.

Table 2. Optimized design parameters of four machines.

Items	$N_f = 2$	$N_f = 3$	$N_f = 4$	$N_f = 5$
FMPs pitch ratio, τ_f/τ_s	1.3	1.2	1.15	1.1
Isolation tooth width ratio, τ_g/τ_s	0.95	0.85	0.8	0.8
Height of FMPs, H_f (mm)	5.5	6	5.5	5
Magnet thickness, H_m (mm)	13.5	10	7.5	6.5

4.1. Air Gap Flux Density

FMPs are non-uniformly distributed after optimization, so Z_s in Eq. (3) will be replaced by Z_a, which means that the harmonics can be rewritten as follows:

$$P'_{m,n} = |mP_r \pm nZ_a| \quad m = 1, 3, 5, \ldots \quad n = 0, 1, 2, \ldots \tag{7}$$

The no-load air gap flux density and fourier analysis of the four machines are illustrated in Figs. 7(a)–(h). It can be seen that the harmonic orders of four machines satisfy Eq. (7), indicating that they all operate according to the principle of flux modulation effect. Furthermore, the amplitudes of fundamental harmonics, i.e., 13th, 19th, 25th, and 31st, are almost unchanged with the increase of N_f, while those of residual working harmonics which are marked in the figure decrease gradually. Theoretically, the weakening of flux modulation effect will lead to the reduction of torque. However, the value of torque is the largest when $N_f = 4$. That is mainly because the torque is proportional to the product of $P_r/P_r \pm iZ_a$ and the amplitude of air gap flux density, as presented in Eq. (8). The former increases along with the increase of N_f, and the latter decreases with the increase of N_f. Therefore, there must

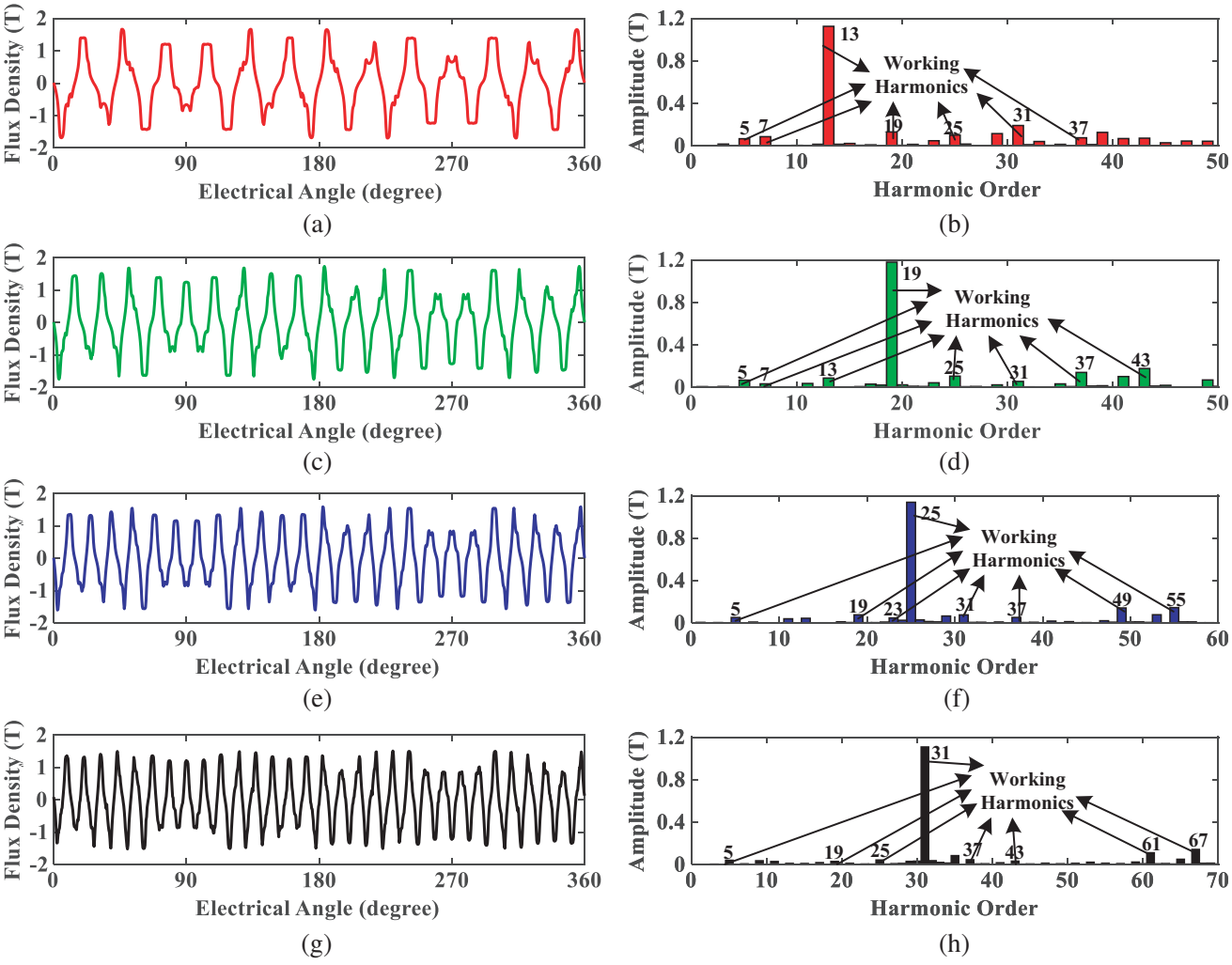

Figure 7. No-load air gap flux density of four machines and fourier analysis. (a) $N_f = 2$, flux density. (b) $N_f = 2$, spectrums. (c) $N_f = 3$, flux density. (d) $N_f = 3$, spectrums. (e) $N_f = 4$, flux density. (f) $N_f = 4$, spectrums. (g) $N_f = 5$, flux density. (h) $N_f = 5$, spectrums.

be an optimal N_f to maximize the torque.

$$T_e = 3\sqrt{2}DLNI_{rms}k_w \sum_{i=0,1,2,3} \left| \frac{P_r}{P_r \pm iZ_a} B_{(P_r \pm iZ_a)} \right| \tag{8}$$

where D is the stator inner diameter, L the axial length, N the winding turns per phase, k_w the winding factor, I_{rms} the rated current, B the amplitude of flux density harmonic, and the subscript $(P_r \pm iZ_a)$ of B indicates the pole pair number of the corresponding harmonic.

4.2. No-Load Back-EMF

Figure 8 depicts the back-EMF waveforms and Fourier analysis of four machines at rated speed. It can be found that with the increase of N_f, the amplitude of the fundamental component of back EMF first increases and then decreases. When $N_f = 4$, the amplitude is the largest, which is similar to the above torque. In addition, the harmonic distortion rate decreases gradually albeit with increased N_f, and it is the smallest when $N_f = 5$.

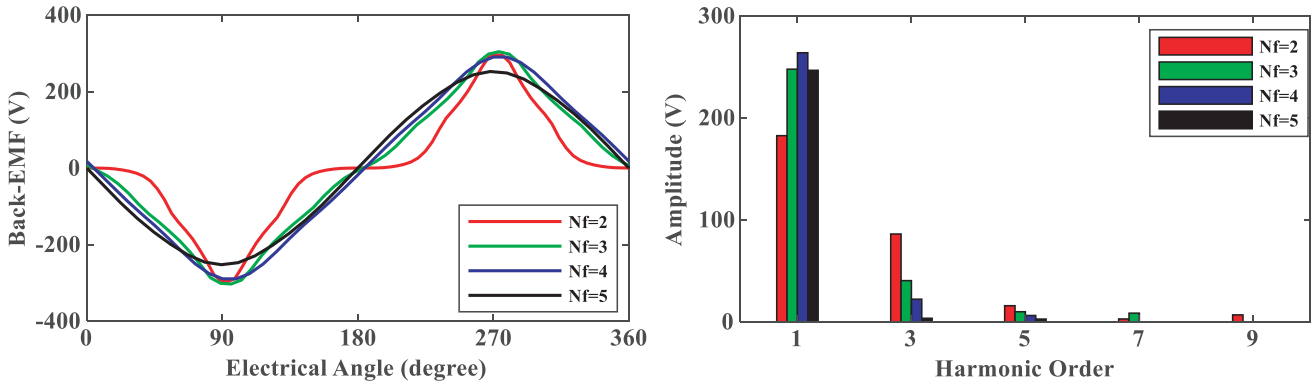

Figure 8. No-load back-EMF and fourier analysis of four machines at 600 r/min. (a) Waveforms. (b) Spectrums.

4.3. Torque Performance

The cogging torque and output torque of the four machines are revealed in Fig. 9. It can be concluded that the cogging torque periods of four machines are 6 in an electrical cycle. Moreover, the cogging

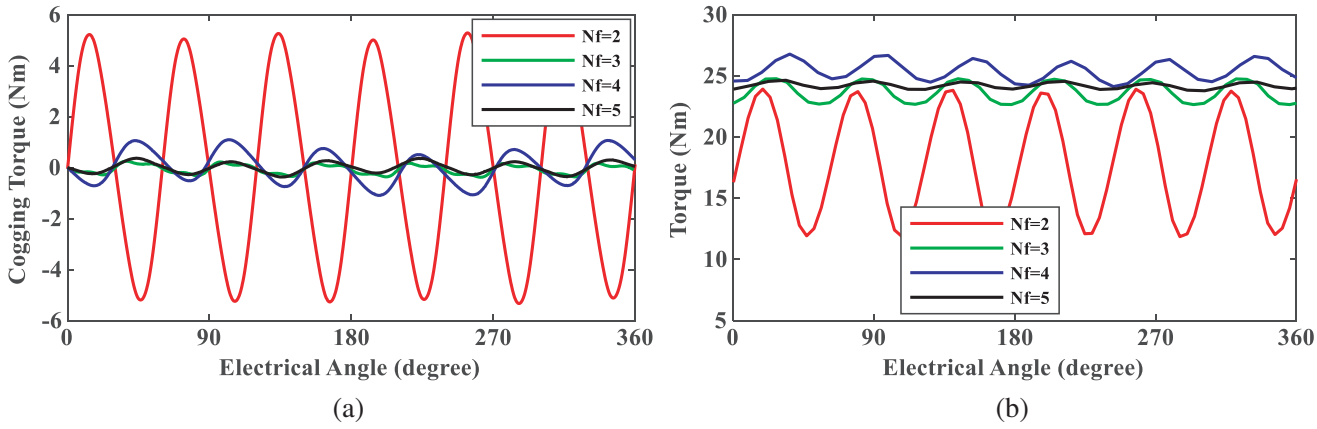

Figure 9. Cogging torque and output torque of four machines. (a) Cogging torque. (b) Output torque.

torque is the largest when $N_f = 2$, while when $N_f = 3$ and $N_f = 5$, it is smaller due to the larger $LCM(2P_r, Z_s)$. In addition, the output torque is the largest when $N_f = 4$. The torque ripples of four machines are 68.1%, 9.8%, 10.7%, and 3.7%, respectively, mainly because the main component of torque ripple is cogging torque.

4.4. Fault Tolerant Capability

The self inductance and coupling coefficient which is defined as the ratio of mutual inductance to self inductance of four machines are shown in Fig. 10(a). As can be seen, the larger the N_f is, the larger the self inductance is. In addition, the coupling coefficient gradually increases with increased N_f, but none of them exceeds 5%, indicating the weak coupling effects of four machines. Moreover, the single-phase short-circuit current is presented in Fig. 10(b). It can be noted that the short-circuit current increases with rotor speed in the beginning, owing to the stronger flux linkage. After it reaches the maximum value, the short-circuit current remains constant. The larger the N_f is, the smaller the short-circuit current is, which means that selecting large N_f is beneficial for suppressing short-circuit current.

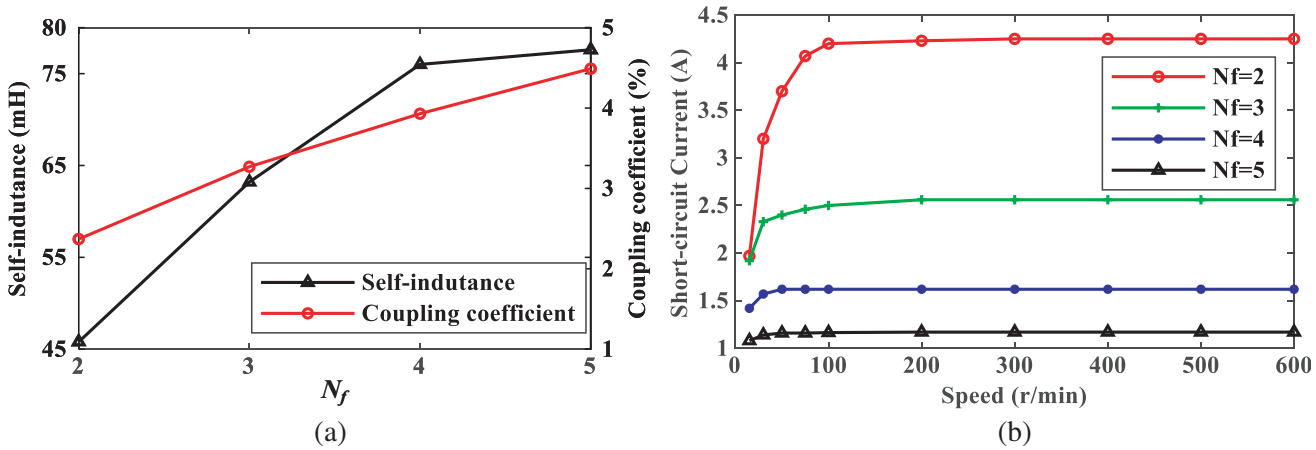

Figure 10. Inductance and short-circuit current of four machines. (a) Self-inductance and coupling coefficient. (b) Short-circuit current waveforms.

4.5. Losses and Efficiency

Without considering other losses such as mechanical loss, the efficiency of SA-FTPMV-RDM which is supplied with rated current of 1.5 A in BLAC mode can be approximated as:

$$\eta = \frac{P_{\text{out}}}{P_{\text{out}} + P_{Cu} + P_{\text{core}} + P_{ec}} \tag{9}$$

where P_{out} is the output power, P_{Cu} the copper loss, P_{core} the core loss, and P_{ec} the eddy current loss. The variation curves of core loss, eddy current loss, and efficiency with speed of four machines are shown in Figs. 11(a)–(c). It can be found that the core loss increases rapidly with the increase of speed, and the larger the N_f is, the larger the core loss is due to the greater frequency. Moreover, the variation law of eddy current loss versus speed is similar to that of core loss, but its value is less than that of core loss. The efficiencies of four machines increase gradually with speed. When $N_f = 4$, the efficiency is the largest owing to its largest torque.

4.6. Influence of Skew Model

According to the above analysis, the torque ripple is relatively large when $N_f = 2$ and 4, which mainly comes from cogging torque and THD of back EMF. The influence of rotor skew on cogging torque and back EMF of four machines is analyzed, as shown in Fig. 12. It can be found that there is an optimal

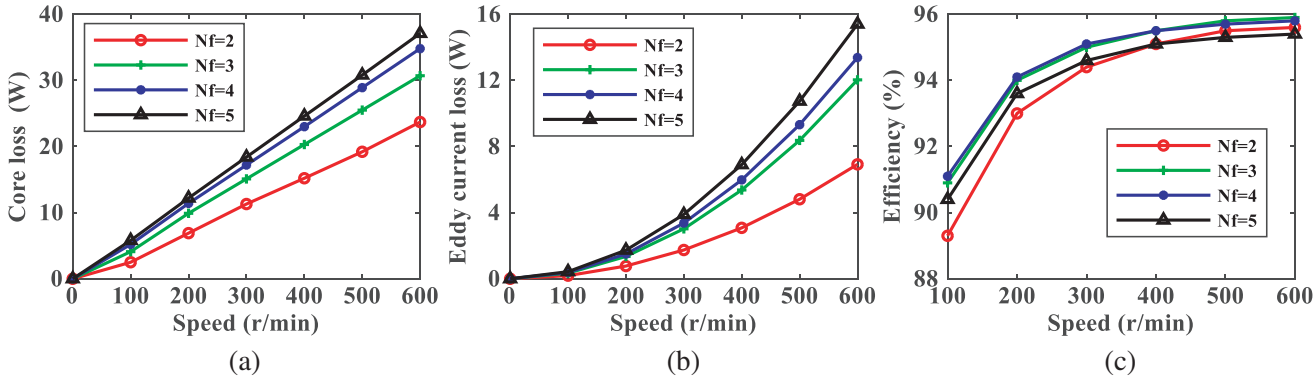

Figure 11. Curves of core loss, eddy current loss and efficiency with speed of four machines. (a) Core loss versus speed. (b) Eddy current loss versus speed. (c) Efficiency versus speed.

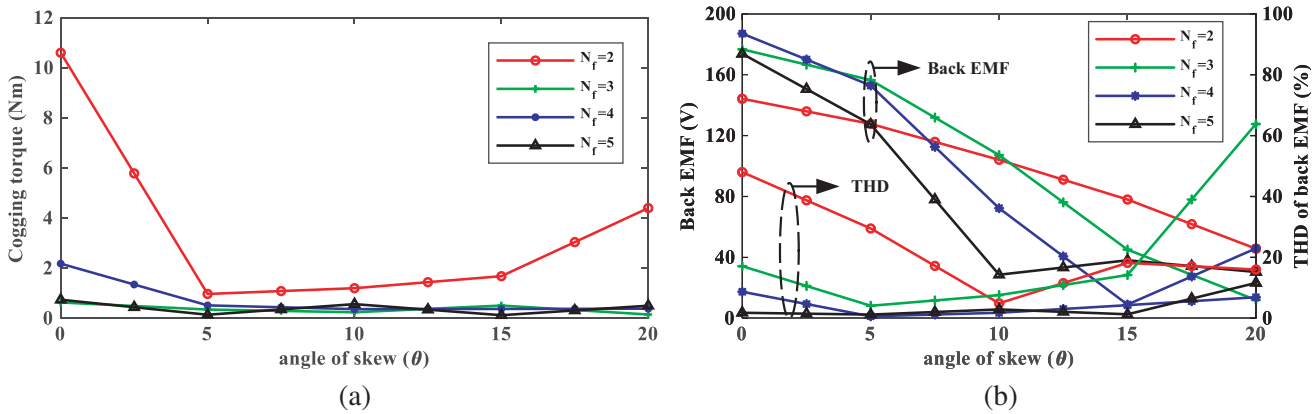

Figure 12. Influence of rotor skew on cogging torque and EMF of four machines. (a) Cogging torque. (b) Back EMF.

angle for the four machines to minimize the cogging torque and THD, so as to reduce the torque ripple. However, the amplitude of back EMF decreases significantly with angle. Therefore, increasing torque density and reducing torque ripple need to be considered comprehensively.

5. CONCLUSION

The combination of PMVM and RDT enriches the types of rim propulsion machines for ship integrated propeller and provides a new idea for the research of RDT with high torque density and strong fault tolerance. In this paper, the performance of SA-FTPMV-RDM with different numbers of FMPs is investigated. The parameter scanning method is used to optimize the four machines with $N_f = 2$, 3, 4, and 5, and the optimal stator and rotor parameters are obtained. The electromagnetic performances of four machines are compared by FEA. the following conclusions are drawn:

1) For six-phase 12-slot SA-FTPMV-RDM, there is an optimal number of FMPs to maximize the torque, and the number is 4 in this paper.

2) In order to obtain the maximum torque, the four machines have the optimal FMPs pitch ratio, isolation tooth width ratio, height of FMPs, and permanent magnet thickness.

3) A comprehensive consideration is required to obtain the maximum torque and minimum torque ripple. Choosing large N_f is beneficial for limiting short-circuit current.

ACKNOWLEDGMENT

This work was supported by the National Natural Science Foundation of China under Project 51777024.

REFERENCES

1. Yahamoto, T., M. Izumi, M. Yokoyama, and K. Umemoto, "Electric propulsion motor development for commercial ships in Japan," *Proceedings of the IEEE*, Vol. 103, No. 12, 2333-2343, 2015.
2. Yan, X., X. Liang, W. Ouyang, et al., "A review of progress and applications of ship shaft-less rim-driven thrusters," *Ocean Engineering*, Vol. 144, 142–156, 2017.
3. Li, Y., B. Song, Z. Mao, and W. Tian, "Analysis and optimization of the electromagnetic performance of a novel stator modular ring drive thruster motor," *Energies*, Vol. 11, No. 6, 1–23, 2018.
4. Hassannia, A. and A. Darabi, "Design and performance analysis of superconducting rim-driven synchronous motors for marine propulsion," *IEEE Transactions on Applied Superconductivity*, Vol. 24, No. 1, 40–46, 2014.
5. Ojaghlu, P. and A. Vahedi, "Specification and design of ring winding axial flux motor for rim-driven thruster of ship electric propulsion," *IEEE Transactions on Vehicular Technology*, Vol. 68, No. 2, 1318–1326, 2019.
6. Wu, F. and A. M. El Refaie, "Permanent magnet vernier machine: A review," *IET Electric Power Applications*, Vol. 13, No. 2, 127–137, 2019.
7. Liu, C. and K. T. Chau, "Electromagnetic design and analysis of double-rotor flux-modulated permanent-magnet machines," *Progress In Electromagnetics Research*, Vol. 131, 81–97, 2012.
8. Wu, L., R. Qu, D. Li, et al., "Influence of pole ratio and winding pole numbers on performance and optimal design parameters of surface permanent-magnet vernier machines," *IEEE Transactions on Industry Applications*, Vol. 51, No. 5, 3707–3715, 2015.
9. Xu, L., G. Liu, W. Zhao, and J. Ji, "Hybrid excited vernier machines with all excitation sources on the stator for electric vehicles," *Progress In Electromagnetics Research M*, Vol. 46, 113–123, 2016.
10. Toba, A. and T. A. Lipo, "Generic torque-maximizing design methodology of surface permanent-magnet vernier machine," *IEEE Transactions on Industry Applications*, Vol. 36, No. 6, 1539–1546, 2000.
11. Zhou, H., W. Tao, C. Zhou, et al., "Consequent pole permanent magnet vernier machine with asymmetric air-gap field distribution," *IEEE Access*, Vol. 7, 109340–109348, 2019.
12. Liu, G., M. Shao, W. Zhao, J. Ji, Q. Chen, and Q. Feng, "Modeling and analysis of halbach magnetized permanent-magnet machine by using lumped parameter magnetic circuit method," *Progress In Electromagnetics Research M*, Vol. 41, 177–188, 2015.
13. Liu, W. and T. A. Lipo, "Analysis of consequent pole spoke type vernier permanent magnet machine with alternating flux barrier design," *IEEE Transactions on Industry Applications*, Vol. 54, No. 6, 5918–5929, 2018.
14. Kim, B. and T. A. Lipo, "Analysis of a PM vernier motor with spoke structure," *IEEE Transactions on Industry Applications*, Vol. 52, No. 1, 217–225, 2016.
15. Zou, T., D. Li, R. Qu, et al., "Advanced high torque density PM vernier machine with multiple working harmonics," *IEEE Transactions on Industry Applications*, Vol. 53, No. 6, 5295–5304, 2017.
16. Xu, L., W. Zhao, G. Liu, and C. Song, "Design optimization of a spoke-type permanent-magnet vernier machine for torque density and power factor improvements," *IEEE Transactions on Vehicular Technology*, Vol. 68, No. 4, 3446–3456, 2019.